Dynamic State Estimation Based Protection on Series Compensated Transmission Lines

Yu Liu, *Student Member, IEEE*, A. P. Sakis Meliopoulos, *Fellow, IEEE*, Rui Fan, *Student Member, IEEE*, Liangyi Sun, *Student Member, IEEE*, and Zhenyu Tan, *Student Member, IEEE*

***Abstract*—Series compensated transmission lines challenge legacy protection schemes. In this paper, a dynamic state estimation based protection (EBP) method is proposed to address these challenges. The method requires GPS synchronized measurements at both ends of the line and a high-fidelity model of the protection zone. The paper presents the dynamic model of the protection zone and its impact on the performance of the protection scheme. Numerical simulations show that the method can correctly identify faults, independently of position and type. The paper also compares the proposed method versus legacy protection functions such as distance protection and line differential protection. The comparison shows faster detection of internal faults, immunity to current inversion caused by series capacitors (SCs) and improved detection sensitivity for high-impedance faults.**

***Index Terms*—Estimation based protection (EBP), high impedance faults, series compensated lines.**

I. Introduction

TRANSMISSION lines are important components of modern power systems. With ever larger demand for power transmission, transmission systems are evolving with more complexity. One way to increase transmission capability and improve stability is to add Series Capacitors (SCs) to form series compensated lines. Appropriately designed, they can also reduce losses and damp sub-synchronous oscillations [1], [2].

In series compensated lines, protection challenges are caused by the capacitive impedance of SCs that interrupts the continuous inductive impedance of transmission lines. Fig. 1 depicts an example series compensated transmission system, with SCs at M side of MN line. Faults F_1 and F_2 near the M terminal of the line are considered as examples. There are two possible locations of the relay near SCs [3], [6] that would be covered in the paper: bus-side installation (relay II) and line-side installation (relay II').

Legacy protection of the series compensated transmission line MN may experience limitations such as:

Manuscript received April 16, 2016; revised July 25, 2016 and October 8, 2016; accepted November 5, 2016. Date of publication November 29, 2016; date of current version August 22, 2017. This work was supported by the Electric Power Research Institute (PERC), PSERC, New York Power Authority, and New York State Energy Research and Development Authority. Paper no. TPWRD-00472-2016.

The authors are with the Electrical and Computer Engineering, Georgia Institute of Technology, Atlanta, GA 30327 USA (e-mail: yliu400@gatech.edu; sakis.m@gatech.edu; rfan7@gatech.edu; lsun30@gatech.edu; ztan@gatech.edu).

Color versions of one or more of the figures in this paper are available online at http://ieeexplore.ieee.org.

Digital Object Identifier 10.1109/TPWRD.2016.2633410

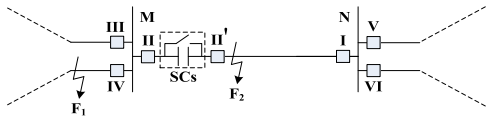

Fig. 1. Series Compensated Transmission Line.

1) **Overcurrent protection and distance protection** at relay I may incorrectly trip for fault F_1, because SCs reduce the impedance between F_1 and relay I. For example, a distance protective relay I may "see" the fault at the middle of the line and incorrectly trip the line if the line is 50% compensated. To avoid this type of mis-operation, the protection zone of overcurrent protection and distance protection should be shortened [4] thus desensitizing the relays. Additionally, protection schemes of both relays II and II' cannot distinguish between fault F_1 and F_2, therefore relay II cannot operate during fault F_2 and relay II' will mis-operate during fault F_1. For similar reasons, **directional element of directional overcurrent protection** at relay II may miss fault F_2, because of current inversion due to capacitive impedance between relay II and F_2 [5]; directional element at relay II' may operate for fault F_1.
2) **Pilot distance protection** scheme may not fully protect the compensated line as well. For bus-side relay installation, the scheme may not trip fault F_2, if relay I cannot cover the total length of the line and relay II will 'see' a capacitive calculated impedance. For line-side relay installation, the scheme may mis-operate during fault F_1.
3) **Direction comparison scheme** may confront similar current inversion problems. For example, relay I and II may detect same direction during fault F_2, and incorrectly neglect this internal fault.
4) **Line differential protection** is one of the most effective protection schemes. However, there still exist some deficits. (a) Current inversion in some situations may lead to failure of differential protection [6]. (b) Long series compensated EHV transmission lines exhibit large capacitance and corresponding large capacitive current, which decreases the sensitivity of differential protection and makes it difficult to detect high impedance faults [7]. (c) To improve sensitivity, use of negative or zero sequence current has been applied as well as compensation for line charging current [6], [16]. These methods and settings are based on sequence models which are approximate and may result in less sensitivity.

Legacy protection functions trip when the calculated results enter the relay characteristic. However, the characteristic does not precisely cover all faults in the entire protection zone due to measurement errors, model errors and unusual fault conditions. Therefore, it is desired to develop methods that are more sensitive, more accurate, do not require complex settings and are preferably free of coordination with other protection functions. We propose a Dynamic State **E**stimation **B**ased **P**rotection (EBP) that possesses the mentioned characteristics [8]–[11]. The main idea of this scheme is to monitor the consistency between the measurements and the dynamic model and quantify this consistency with the probability of goodness of fit (or confidence level). The method requires a high fidelity dynamic model of the protection zone, a set of measurements and a dynamic state estimation algorithm. The dynamic model is constructed from the differential and algebraic equations that capture the physics of the protection zone. Actual measurements are expressed as mathematical functions of the state variables of the dynamic model. In addition, virtual and derived measurements are identified based on the topology of the protection zone. These measurements are added to the measurement set. Given the mathematical model of the measurement set, well known dynamic state estimation algorithms are applied to provide the probability of goodness of fit of the measurements and the dynamic model; this probability is referred to as confidence level.

In this paper, the EBP approach is proposed to protect series compensated lines. A systematic way to derive the model of the protected component is introduced. The performance of EBP relays is verified by numerical simulations.

II. The Algebraic Companion Device Model

EBP protection requires a high fidelity dynamic model of the protection zone. We construct this model as a mathematical object with a specific syntax. For each component of the protection zone, the Quadratized Dynamic Model (QDM) is developed. Next, the QDM of each component is integrated using the quadratic integration method, yielding the Algebraic Quadratic Companion Form (AQCF) of each component. Finally, using the AQCF of the components, the AQCF model of the protection zone is computed. The process is described next and an example is given in Appendix A.

A. Device QDM

Each component satisfies specific physical laws. The physical laws are described via a set of differential and algebraic equations. If the equations exhibit nonlinearities higher than second order, they are "quadratized" by the introduction of additional variables. The quadratized model is then cast into a standard syntax, as follows:

$$\begin{aligned}
\boldsymbol{i}(t) &= \boldsymbol{Y}_{eqx1}\boldsymbol{x}(t) + \boldsymbol{D}_{eqxd1}\frac{d\boldsymbol{x}(t)}{dt} + \boldsymbol{C}_{eqc1} \\
\mathbf{0} &= \boldsymbol{Y}_{eqx2}\boldsymbol{x}(t) + \boldsymbol{D}_{eqxd2}\frac{d\boldsymbol{x}(t)}{dt} + \boldsymbol{C}_{eqc2} \\
\mathbf{0} &= \boldsymbol{Y}_{eqx3}\boldsymbol{x}(t) + \left\{ \begin{array}{c} \vdots \\ \boldsymbol{x}(t)^T \left\langle \boldsymbol{F}^i_{eqxx3} \right\rangle \boldsymbol{x}(t) \\ \vdots \end{array} \right\} + \boldsymbol{C}_{eqc3}
\end{aligned} \quad (1)$$

where $\boldsymbol{x}(t)$and $\boldsymbol{i}(t)$ represent the states and the current measurements of the model, respectively; other matrices ($\boldsymbol{Y}$, $\boldsymbol{D}$, $\boldsymbol{F}$ and $\boldsymbol{C}$) are coefficient matrices. Usually terminal voltages are included in $\boldsymbol{x}(t)$as well as other internal states.

B. Device QDM to Device AQCF

Equations (1) are numerically integrated to convert the differential equations into algebraic equations. For this purpose, we use the quadratic integration method [12] over a time step of $2\Delta t$. Specifically, the differential equations are integrated over the two intervals $[t-2\Delta t, t]$ and $[t-2\Delta t, t_m]$, where Δt is the sampling interval, and $t_m = t - \Delta t$. This process converts (1) into the following Algebraic Quadratic Companion Form (AQCF):

$$\begin{aligned}
\left\{ \begin{array}{c} \boldsymbol{i}(t) \\ \mathbf{0} \\ \mathbf{0} \\ \boldsymbol{i}(t_m) \\ \mathbf{0} \\ \mathbf{0} \end{array} \right\} &= \boldsymbol{Y}_{\mathrm{eqx}}\boldsymbol{x}(t,t_m) + \left\{ \begin{array}{c} \vdots \\ \boldsymbol{x}(t,t_m)^T \left\langle \boldsymbol{F}^i_{\mathrm{eqx}} \right\rangle \boldsymbol{x}(t,t_m) \\ \vdots \end{array} \right\} \\
&\quad + \boldsymbol{b}\,(t-2\Delta t) \\
\boldsymbol{b}(t-2\Delta t) &= \boldsymbol{N}_{\mathrm{eqx}} \cdot \boldsymbol{x}(t-2\Delta t) + \boldsymbol{M}_{\mathrm{eq}} \cdot \boldsymbol{i}(t-2\Delta t) \\
&\quad + \boldsymbol{K}_{\mathrm{eq}}
\end{aligned} \quad (2)$$

where $\boldsymbol{x}(t,t_m) = [\,\boldsymbol{x}(t)\ \boldsymbol{x}(t_m)\,]^T$; each element on the left hand side of (2), i.e. $\boldsymbol{i}(t)$, $\mathbf{0}$, $\mathbf{0}$, $\boldsymbol{i}(t_m)$, $\mathbf{0}$, $\mathbf{0}$, is a vector with an appropriate dimension; and $\boldsymbol{Y}_{\mathrm{eqx}}$, $\boldsymbol{F}^i_{\mathrm{eqx}}$, $\boldsymbol{N}_{\mathrm{eqx}}$, $\boldsymbol{M}_{\mathrm{eq}}$, and $\boldsymbol{K}_{\mathrm{eq}}$ can be directly calculated from the coefficient matrices in (1) [10], [11]. Note that the AQCF model consists of six sets of equations.

C. Protection Zone AQCF

We focus on the protection of a series compensated line which consists of the line and the series capacitors. The model of this protection zone in AQCF format can be developed in one of the following ways: (a) first the line and series capacitor equations are cast in the format of (1) and then integrated with quadratic integration [12]. (b) the line equations are first developed in the format of (1) and then integrated to provide the line AQCF model. The same procedure is applied to the series capacitors yielding the AQCF model of the series capacitors. Subsequently, the two AQCF models are combined to provide the AQCF model of the protection zone consisting of the line and the series capacitors. This process involves the application of Kirchhoff Current Law (KCL) at each interface node between the line and the series capacitors (standard circuit analysis). Either (a) or (b) procedure yields the same AQCF model for the series compensated line protection zone.

The line is modeled as a multi-section transmission line where each section is represented with a generalized π-equivalent model. The length of each section is chosen to be about half the travel distance of electromagnetic waves for one sampling interval; it is well known that this selection increases the accuracy of the line model. Note that in this case the protection

zone model consists of the series capacitors and the sections of the line. The QDMs of these components are presented in Appendix A. Subsequently, the QDMs of the capacitors and line sections are integrated yielding the AQCF models which are then combined to provide the SC and line AQCF model.

III. The AQCF Measurement Model

Each measurement is mathematically expressed in terms of the states of the protection zone AQCF model. Each measurement model is directly extracted from the AQCF model. For example, the model of a current measurement at time t at a terminal of a protection zone is simply the equation of the protection zone AQCF model that provides this current in (2). The syntax of each measurement is provided in (3) below.

$$\begin{aligned}
\boldsymbol{z}\,(t) &= \boldsymbol{Y}_{1m,x}\boldsymbol{x}\,(t,t_m) + \left\{\begin{array}{c}\vdots\\ \boldsymbol{x}(t,t_m)^T\boldsymbol{F}^i_{1m,x}\boldsymbol{x}\,(t,t_m)\\ \vdots\end{array}\right\} \\
&\quad +\ \boldsymbol{C}_{1m}\,(t-2\Delta t) \\
\boldsymbol{C}_{1m}\,(t-2\Delta t) &= \boldsymbol{N}_{1m,x}\boldsymbol{x}(t-2\Delta t) + \boldsymbol{M}_{1m}i(t-2\Delta t) \\
&\quad +\ \boldsymbol{K}_{1m} \\
\boldsymbol{z}\,(t_m) &= \boldsymbol{Y}_{2m,x}\boldsymbol{x}\,(t,t_m) + \left\{\begin{array}{c}\vdots\\ \boldsymbol{x}(t,t_m)^T\boldsymbol{F}^i_{2m,x}\boldsymbol{x}\,(t,t_m)\\ \vdots\end{array}\right\} \\
&\quad +\ \boldsymbol{C}_{2m}\,(t-2\Delta t) \\
\boldsymbol{C}_{2m}\,(t-2\Delta t) &= \boldsymbol{N}_{2m,x}\boldsymbol{x}(t-2\Delta t) + \boldsymbol{M}_{2m}i(t-2\Delta t) \\
&\quad +\ \boldsymbol{K}_{2m}
\end{aligned} \tag{3}$$

We represent all the measurements with the vector $\boldsymbol{z}(t,t_m) = [\,\boldsymbol{z}(t)\ \boldsymbol{z}(t_m)\,]^T$ and the compact notation $\boldsymbol{z}(t,t_m) = h(\boldsymbol{x}(t,t_m))$. Measurements can be categorized as follows. (a) Actual measurements represent measurements that are taken with actual meters with VTs, CTs, and other sensors. The standard deviation of the measurement error is determined by the corresponding meter. (b) Virtual measurements represent quantities that are known from physical laws, for example KCL at a node of the protection zone. (c) Derived measurements are quantities which are equal to another quantity (by virtue of a physical law) for which we have an actual measurement (for example, the phase A current of the series capacitor and the phase A current in the line). If a measurement of the line current is available but not the capacitor, we introduce a current measurement for the capacitor as a derived measurement. (d) Pseudo measurements represent physical quantities for which we do not have measurements but we know the range of expected values. The addition of virtual, derived and pseudo measurements makes the measurement set larger and increases the measurement redundancy.

IV. EBP Method

EBP uses Dynamic State Estimation (DSE), which estimates the states $\boldsymbol{x}(t,t_m)$ ($m_{\mathbf{x}}$ states) from redundant measurements $\boldsymbol{z}(t,t_m)$ ($m_{\mathbf{z}}$ measurements $> m_{\mathbf{x}}$). The DSE executes once the measurement samples from time t and t_m are available (two sampling intervals). There are several DSE algorithms for estimating the state $\hat{\boldsymbol{x}}(t,t_m)$. Concise descriptions of two methods are provided below.

Constraint Optimization method treats virtual measurements as constraints to form a constraint optimization problem:

$$\begin{aligned}
\text{Min } J &= \left(h_c(\boldsymbol{x}(t,t_m)) - \boldsymbol{z}_c(t,t_m)\right)^T\boldsymbol{W}_c\left(h_c(\boldsymbol{x}(t,t_m))\right. \\
&\quad \left. -\ \boldsymbol{z}_c(t,t_m)\right) \\
\text{Subject To:}\quad & \mathbf{0} = g_c(\boldsymbol{x}(t,t_m))
\end{aligned} \tag{4}$$

where $g_c(\boldsymbol{x}(t,t_m))$ corresponds to virtual measurements (constraints), $\boldsymbol{z}_c(t,t_m)$ and $h_c(\boldsymbol{x}(t,t_m))$ correspond to the remaining measurements (actual, derived and pseudo), $\boldsymbol{W}_c = \mathrm{diag}\{1/\sigma_1^2, 1/\sigma_2^2, \cdots\}$, and σ_i is the standard deviation of each measurement in the set $\boldsymbol{z}_c(t,t_m)$.

The best state estimate $\hat{\boldsymbol{x}}(t,t_m)$ is computed by the method of Lagrangian multipliers given with the following iterative algorithm until convergence:

$$\begin{aligned}
\begin{bmatrix}\hat{\boldsymbol{x}}(t,t_m)^{v+1}\\ \hat{\boldsymbol{\lambda}}(t,t_m)^{v+1}\end{bmatrix} &= \begin{bmatrix}\hat{\boldsymbol{x}}(t,t_m)^{v}\\ \hat{\boldsymbol{\lambda}}(t,t_m)^{v}\end{bmatrix} - \begin{bmatrix}\boldsymbol{H}_c{}^T\boldsymbol{W}_c\boldsymbol{H}_c & \boldsymbol{G}_c{}^T\\ \boldsymbol{G}_c & \mathbf{0}\end{bmatrix}^{-1} \\
&\quad \times \begin{bmatrix}\boldsymbol{H}_c{}^T\boldsymbol{W}_c\left(h_c(\hat{\boldsymbol{x}}(t,t_m)^v) - \boldsymbol{z}_c(t,t_m)\right) + \boldsymbol{G}_c{}^T\hat{\boldsymbol{\lambda}}(t,t_m)^v\\ g_c(\hat{\boldsymbol{x}}(t,t_m)^v)\end{bmatrix}
\end{aligned} \tag{5}$$

where the Jacobian matrices $\boldsymbol{H}_c = \partial h_c(\boldsymbol{x})/\partial\boldsymbol{x}$, $\boldsymbol{G}_c = \partial g_c(\boldsymbol{x})/\partial\boldsymbol{x}$, and $\boldsymbol{\lambda}(t,t_m)$ is the Lagrangian multiplier.

Unconstraint Optimization method treats virtual measurements the same as all other measurements, except that they have very small standard deviation. The unconstraint optimization problem is:

$$\begin{aligned}
\text{Min } J = &\ \left(h(\boldsymbol{x}(t,t_m)) - \mathbf{z}(t,t_m)\right)^T\boldsymbol{W}\left(h(\boldsymbol{x}(t,t_m))\right. \\
&\left. -\ \boldsymbol{z}(t,t_m)\right)
\end{aligned} \tag{6}$$

where $\boldsymbol{z}(t,t_m)$ and $h(\boldsymbol{x}(t,t_m))$ correspond to all measurements, $\boldsymbol{W} = \mathrm{diag}\{1/\sigma_1^2, 1/\sigma_2^2, \cdots\}$, and σ_i is the standard deviation of measurement i.

The best state estimate $\hat{\boldsymbol{x}}(t,t_m)$ is computed by the following iterative algorithm until convergence:

$$\begin{aligned}
\hat{\boldsymbol{x}}(t,t_m)^{\nu+1} = &\ \hat{\boldsymbol{x}}(t,t_m)^{\nu} - (\boldsymbol{H}^T\boldsymbol{W}\boldsymbol{H})^{-1}\boldsymbol{H}^T\boldsymbol{W} \\
&\times \left(h(\hat{\boldsymbol{x}}(t,t_m)^{\nu}) - \boldsymbol{z}(t,t_m)\right)
\end{aligned} \tag{7}$$

where the Jacobian matrix $\boldsymbol{H} = \partial h(\boldsymbol{x})/\partial\boldsymbol{x}$.

Note that the measurement model (3) includes past history vectors $\boldsymbol{C}_{1m}(t-2\Delta t)$ and $\boldsymbol{C}_{2m}(t-2\Delta t)$, which depend on past history values of states and currents. Algorithmically, there are two options: (a) use estimated values from the previous DSE time step for $\boldsymbol{x}(t-2\Delta t)$ and $\boldsymbol{i}(t-2\Delta t)$ in the calculation of past history vectors $\boldsymbol{C}_{1m}(t-2\Delta t)$ and $\boldsymbol{C}_{2m}(t-2\Delta t)$; (b) use measured values for $\boldsymbol{x}(t-2\Delta t)$ and $\boldsymbol{i}(t-2\Delta t)$

in the calculation of past history vectors, if the corresponding measurements exist (otherwise use estimated values).

Different combinations of these choices were tested. The results suggest that for the EBP application: (a) the unconstraint method converges a little faster than the constraint method; (b) there exists little difference between estimated and measured past history methods. In this paper, unconstraint optimization with estimated past history method is chosen and used for all numerical experiments.

Upon execution of the DSE, the residuals $\hat{\boldsymbol{r}}(t, t_m)$ and normalized residuals $\hat{\boldsymbol{s}}(t, t_m)$ are computed using the estimated state $\hat{\boldsymbol{x}}(t, t_m)$:

$$\hat{\boldsymbol{r}}(t, t_m) = h(\hat{\boldsymbol{x}}(t, t_m)) - \boldsymbol{z}(t, t_m) \tag{8}$$

$$\hat{\boldsymbol{s}}(t, t_m) = \sqrt{\boldsymbol{W}} \cdot \hat{\boldsymbol{r}}(t, t_m) \tag{9}$$

Subsequently, the confidence level $P_{\text{conf}}(t)$, which expresses the probability of goodness of fit between measurements and dynamic model within meter accuracy, is computed from the normalized residuals $\hat{\boldsymbol{s}}(t, t_m)$ [13]:

$$\zeta(t) = \hat{\boldsymbol{s}}(t, t_m)^T \hat{\boldsymbol{s}}(t, t_m) \tag{10}$$

$$P_{\text{conf}}(t) = P\left(\chi^2 \geq \zeta(t)\right) = 1 - P\left(\zeta(t), m_v\right) \tag{11}$$

where $P(\zeta(t), m_v)$ is the probability of χ^2 distribution given $\chi^2 \leq \zeta(t)$ with $m_v = m_{\mathbf{z}} - m_{\mathbf{x}}$ degrees of freedom.

A high confidence level suggests that the measurements and the dynamic model are consistent, while a low confidence level implies that, assuming no instrumentation error, there exists an internal fault. For dependable and secure protection, a user defined time delay for tripping is introduced. We use the following trip logic which includes a user defined delay τ_{delay} and a reset time τ_{reset}:

$$TripValue(\text{t}) = \int_{t-\tau_{\text{reset}}}^{t} \left(1 - P_{\text{conf}}\left(t\right)\right) dt \tag{12}$$

$$Trip(\text{t}) = \begin{cases} 1, & \text{if } TripValue(\text{t}) \geq \tau_{\text{delay}} \\ 0, & \text{if } TripValue(\text{t}) < \tau_{\text{delay}} \end{cases} \tag{13}$$

Above equation guarantees that the trip signal is issued only when the confidence level remains consistently low for a user controlled time period before the trip signal goes to 1.0.

V. Hardware In The Loop Simulation Platform

The proposed EBP relay is tested in the laboratory with hardware in the loop, as shown in Fig. 2. The fault events are simulated in the computer in the far left and the digital waveforms are fed into a bank of D/A converters (NI cDAQ9188). The analog signals are fed into a bank of amplifiers that amplify the signal to standard voltages and currents at the secondary of VTs and CTs. The output of the amplifiers is connected to the input of the merging units (MU). The output of the MUs is connected to the process bus and the setting-less relay software is running in a personal computer (far right) which is connected to the process bus. GPS synchronization is achieved by an optical feed of an IRIG-B signal [17] into the merging units (not shown in figure).

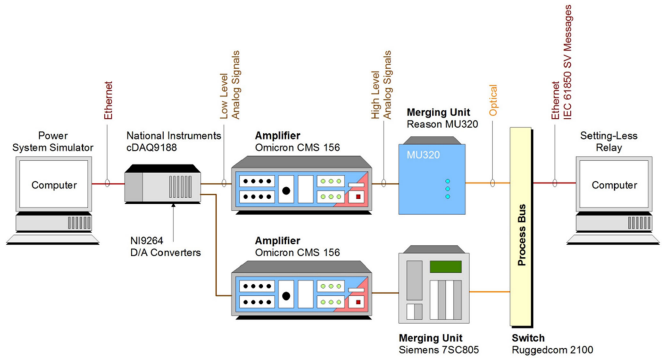

Fig. 2. Hardware in the loop simulation platform.

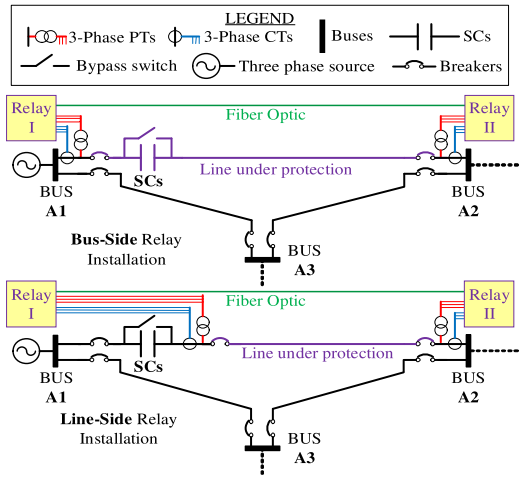

Fig. 3. Example test system: series compensated line, with bus side relay installation and line side relay installation.

TABLE I
Source Impedances

Parameter	Value
Positive sequence impedance	$13.59\angle 86.99^\circ\ \Omega$
Negative sequence impedance	$12.88\angle 86.82^\circ\ \Omega$
Zero sequence impedance	$5.76\angle 82.88^\circ\ \Omega$

Note that the MUs, process bus and setting-less relay computer represent the hardware of the EBP.

VI. Example Application: Series Compensated Lines

We compare the performance of the proposed EBP with typical legacy protection schemes for a series compensated power line. The compensation is located at one terminal of the line. We consider two possible installations of the relay: bus-side installation and line-side installation. Fig. 3 illustrates the power line and the two possible locations of the measurements; the rest of the network is not shown. The line ratings are: 500 kV, 83-mile long, 4330 MVA. The series capacitors are 0.148 mF representing a 42.4% compensation.

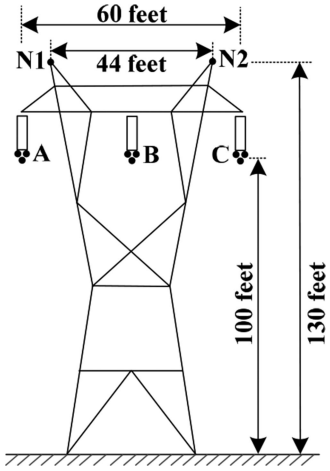

Fig. 4. Tower structure of the transmission line

TABLE II
R, L AND C MATRICES OF THE LINE

Parameter matrices	Value
Series resistance (per mile)	$\begin{bmatrix} 0.104 & 0.089 & 0.089 & 0.088 & 0.088 \\ 0.089 & 0.104 & 0.089 & 0.088 & 0.088 \\ 0.089 & 0.089 & 0.104 & 0.088 & 0.088 \\ 0.088 & 0.088 & 0.088 & 2.357 & 0.087 \\ 0.088 & 0.088 & 0.088 & 0.087 & 2.357 \end{bmatrix}$ Ω/mi
Series inductance (per mile)	$\begin{bmatrix} 2.79 & 1.48 & 1.26 & 1.47 & 1.26 \\ 1.48 & 2.89 & 1.48 & 1.41 & 1.41 \\ 1.26 & 1.48 & 2.79 & 1.26 & 1.47 \\ 1.47 & 1.41 & 1.26 & 5.55 & 1.36 \\ 1.26 & 1.41 & 1.47 & 1.36 & 5.55 \end{bmatrix}$ mH/mi
Shunt capacitance (per mile)	$\begin{bmatrix} 9.01 & -2.11 & -0.75 & -1.33 & -0.50 \\ -2.11 & 9.55 & -2.11 & -0.94 & -0.94 \\ -0.75 & -2.11 & 9.01 & -0.50 & -1.33 \\ -1.33 & -0.94 & -0.50 & 5.52 & -0.58 \\ -0.50 & -0.94 & -1.33 & -0.58 & 5.52 \end{bmatrix}$ nF/mi
Shunt conductance (per mile)	$\mathbf{0}_{5\times5}$ mho/mi

TABLE III
SEQUENCE PARAMETERS OF THE LINE

Parameter	Value
Positive (Negative) sequence series impedance (Z_1)	$42.53\angle 88.34^\circ\ \Omega$
Zero sequence series impedance (Z_0)	$142.71\angle 74.56^\circ\ \Omega$
Positive (Negative) sequence shunt susceptance (Y_1)	$0.341\angle 90.0^\circ\ \text{m}\Omega$
Zero sequence shunt susceptance (Y_0)	$0.186\angle 90.0^\circ\ \text{m}\Omega$

The source impedance is shown inTable I. The tower structure is provided in Fig. 4. The tower footing resistance is 25 ohms and the ground impedance of the substations at the two ends of the line is one ohm. The R, L and C matrices of the transmission line are provided in Table II. The sequence parameters are shown in Table III. The sampling rate is 4800 samples/second. The dynamic state estimation for each time step executes in a fraction of the time between two consecutive samples of streaming data, 416 μs. The typical execution time for this system is 120 μs on a high end personal computer.

Because of space limitation and for comparison purposes with the EBP, we assumed the line is protected with only two

TABLE IV
DISTANCE RELAY SETTINGS (BUS SIDE)

Function	Settings
Line and Ground Distance, Zone 1	$19.72\angle 87.13^\circ\ \Omega$, 0.015 s delay, compensation factor $k = 2.39\angle -19.48^\circ\ \Omega$
Line and Ground Distance, Zone 2	$30.80\angle 87.13^\circ\ \Omega$, 0.15 sdelay, compensation factor $k = 2.39\angle -19.48^\circ\ \Omega$
Line and Ground Distance, Zone 3	$64.08\angle 87.13^\circ\ \Omega$, 0.5 sdelay, compensation factor $k = 2.39\angle -19.48^\circ\ \Omega$

TABLE V
DISTANCE RELAY SETTINGS (LINE SIDE)

Function	Settings
Line and Ground Distance, Zone 1	$34.02\angle 88.34^\circ\ \Omega$, 0.015 s delay, compensation factor $k = 2.39\angle -19.48^\circ\ \Omega$
Line and Ground Distance, Zone 2	$53.16\angle 88.34^\circ\ \Omega$, 0.15 s delay, compensation factor $k = 2.39\angle -19.48^\circ\ \Omega$
Line and Ground Distance, Zone 3	$110.58\angle 88.34^\circ\ \Omega$, 0.5 s delay, compensation factor $k = 2.39\angle -19.48^\circ\ \Omega$

legacy protection functions: (a) distance protection (at side A1), and (b) line differential protection (alpha plane). The settings of the legacy protection functions as well as EBP are provided corresponding to two possible locations of the relay.

Bus-side relay installation, distance protection settings: The distance relay settings are shown in Table IV.

Bus-side relay installation, line differential protection settings (alpha plane) [14]: Zero sequence current differential protection scheme with capacitive charging current compensation is used. The restraint region is between 1/6 to 6, with total angular extent 195°. The relay trip logic is activated when at least one of the following thresholds is exceeded (a) phase current 6 kA, (b) $3I_0$ (zero-sequence) current 500 A, (c) $3I_2$ (negative-sequence) current 500 A. The relay will trip when the trip logic is activated and the ratio falls outside the restraint region, with a delay of 0.015 s.

Bus-side relay installation, EBP settings: For consistency, the intentional delay for the EBP relay is also selected as $\tau_{\text{delay}} = 0.015$ s and the reset time is $\tau_{\text{reset}} = 0.03$ s.

Line-side relay installation, distance protection settings: The distance relay settings are shown in Table V.

Line-side relay installation, line differential protection settings: The settings of the line-side line differential relay are exactly the same as the bus-side line differential relay.

Line-side relay installation, EBP settings: Settings of line-side EBP relay are exactly same as bus-side EBP relay.

We compare the performance of the legacy protection functions to the EBP relay performance for three specific events.

A. Event 1: Low Impedance Phase A-G Internal Fault near Bus A1

A phase A to ground internal fault with 0.4 Ω impedance happens at 1 mile from the side A1 and time 0.5 s. The results are shown in Fig. 5 for the period [0.45 s to 0.55 s].

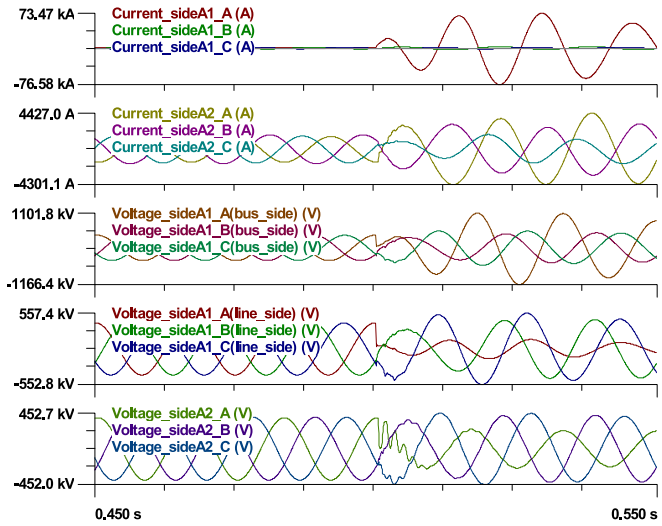

Fig. 5. Current and voltage results of a phase A to ground internal fault near SCs.

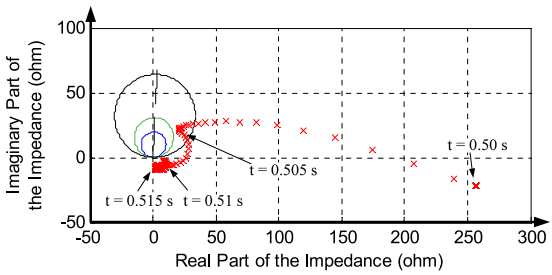

Fig. 6. Trace of impedance during a phase A to ground internal fault near SCs, bus-side relay installation.

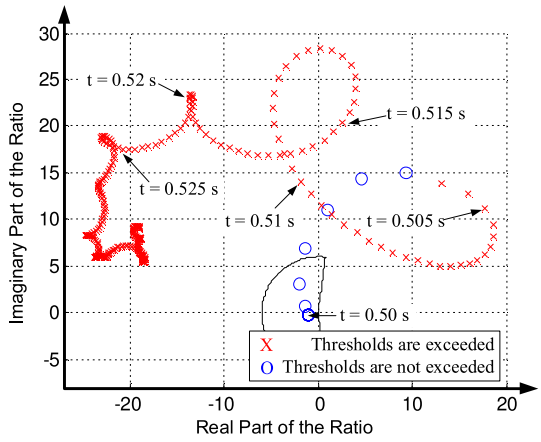

Fig. 7. Trace of the ratios during a phase A to ground internal fault near SCs, bus-side relay installation.

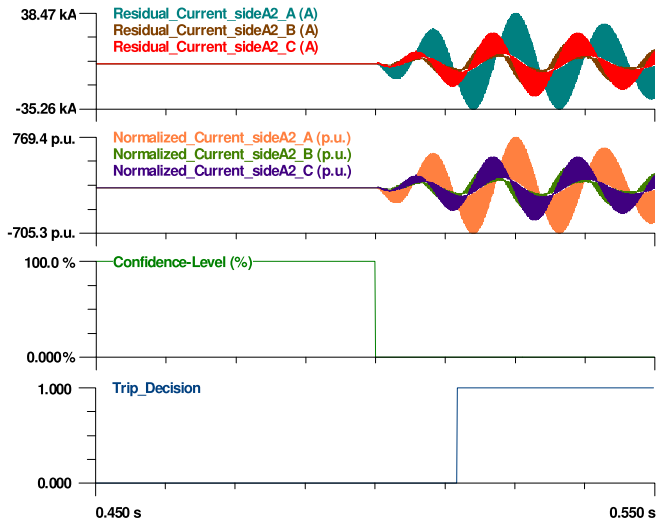

Fig. 8. EBP results of a phase A to ground internal fault near SCs, bus-side relay installation.

Performance of Bus-side Relay Installation

Distance relay: the trace of the impedance "seen" by the relay, superimposed on its characteristic, is shown in Fig. 6. It can be observed that the impedance stays outside the tripping characteristics during the fault due to the capacitive reactance of SCs. Therefore, the distance relay fails to detect this fault.

Line differential protection relay: the phasor ratio trace of zero sequence current, superimposed on the relay characteristic, is shown in Fig. 7. Along the trace, the character 'o' means the thresholds are not exceeded while the character 'x' means the thresholds are exceeded. Prior to the fault, the ratio is near the ideal point $(-1, 0)$, and none of the thresholds are exceeded (with the character 'o'). During the fault, the thresholds are gradually exceeded (transition 'o' to 'x') with the ratio already in the trip zone. The transition (detection) occurs at 0.504 s. The line differential relay trips the line at $0.504 + 0.015$ s $=$ 0.519 s.

EBP relay: The results are depicted in Fig. 8. The first two sets of traces show the residuals and normalized residuals of three-phase currents of side A2. The confidence level and the trip signal are given in the next two traces. The confidence level drops to zero at time 0.5002 s. Thus the fault is detected at 0.5002 s and the line is tripped at 0.5152 s.

Summary: For event 1 and **bus-side relay installation**, the distance relay fails to detect the fault; the line differential relay detects the fault at 0.504 s and trips the line at 0.519 s; the EBP relay detects the fault at 0.5002 s and trips the line at 0.5152 s.

Performance of Line-side relay installation

Distance protection relay: the trace of impedance "seen" by the relay, superimposed on its characteristic, is shown in Fig. 9. It can be observed that the impedance enters zone 1 of the tripping characteristics during the fault. Thus, the distance relay trips the line at $0.509 + 0.015$ s $=$ 0.524 s.

Line differential protection relay: the performance is the same as in Fig. 7. The relay detects the fault at 0.504 s and trips the line at 0.519 s.

EBP relay: The results are depicted in Fig. 10. The detection of the fault happens at 0.5002 s and the relay trips the line at 0.5152 s.

Summary: For event 1 and **line-side relay installation**, the distance relay correctly detects the fault at 0.509 s and trips the

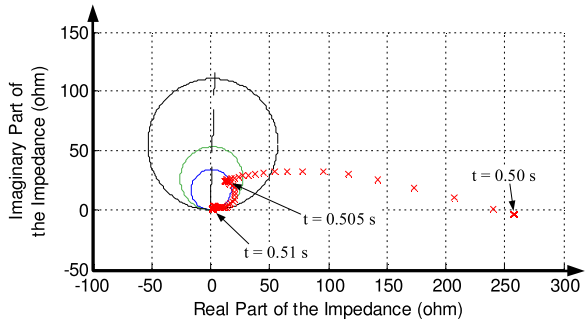

Fig. 9. Trace of impedance during a phase A to ground internal fault near SCs, line-side relay installation.

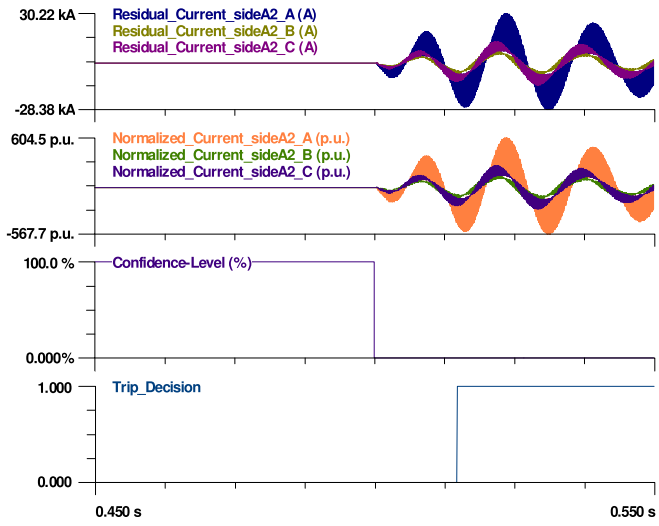

Fig. 10. EBP results of a phase A to ground internal fault near SCs, line-side relay installation.

line at 0.524 s; the line differential relay correctly detects the fault at 0.504 s and trips the line at 0.519 s; the EBP relay detects the fault at 0.5002 s and trips the line at 0.5152 s.

B. Event 2: Bus A1 Low Impedance Phase A-G External Fault

A phase A to ground fault with 0.9 Ω impedance occurs at bus A1 and time 0.5 s. The results are shown in Fig. 11 for the period [0.45 s to 0.55 s].

Performance of Bus-side Relay Installation

Distance protection relay: the impedance "seen" by the relay, superimposed on its characteristic, is shown in Fig. 12. The impedance stays outside the tripping characteristics. Thus, the distance relay correctly ignores this external fault.

Line differential protection relay: the phasor ratio trace of zero sequence current, superimposed on the relay characteristic, is shown in Fig. 13. Prior to the fault, the ratio of zero sequence current is near the ideal point (-1,0), and none of the thresholds are exceeded (with the character 'o'). During the fault, the ratio remains in the restraint region, with some thresholds exceeded (with the character 'x'). Thus, line differential relay correctly ignores this external fault.

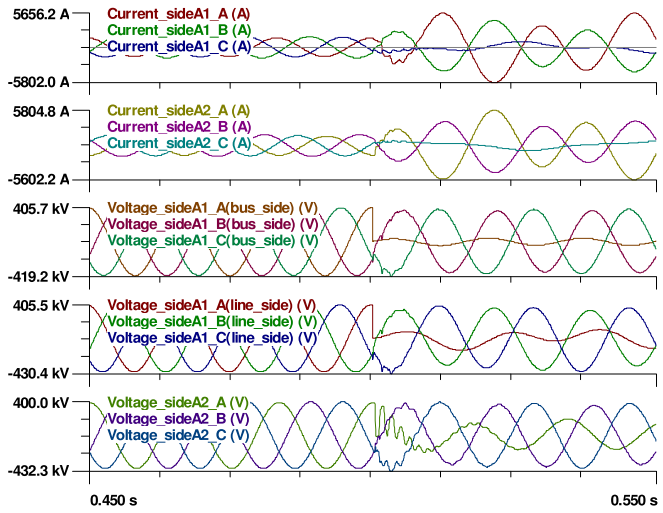

Fig. 11. Current and voltage results of a phase A to ground external fault at bus A1.

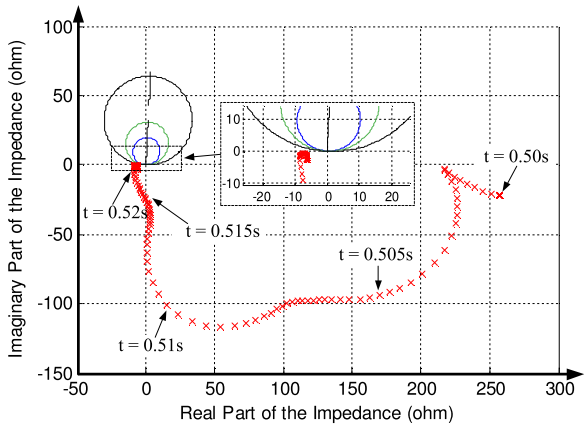

Fig. 12. Trace of impedance during a phase A to ground external fault at bus A1, bus-side relay installation.

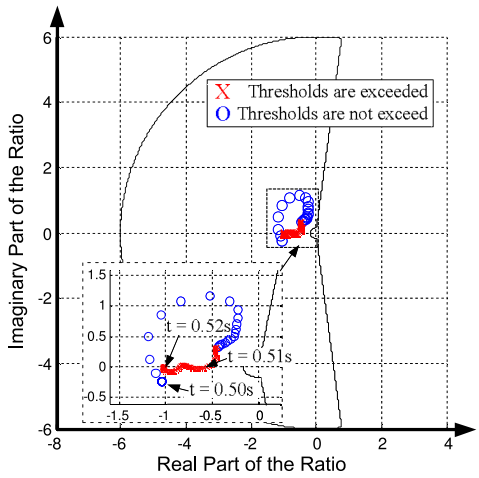

Fig. 13. Trace of the ratios during a phase A to ground external fault at bus A1, bus-side relay installation.

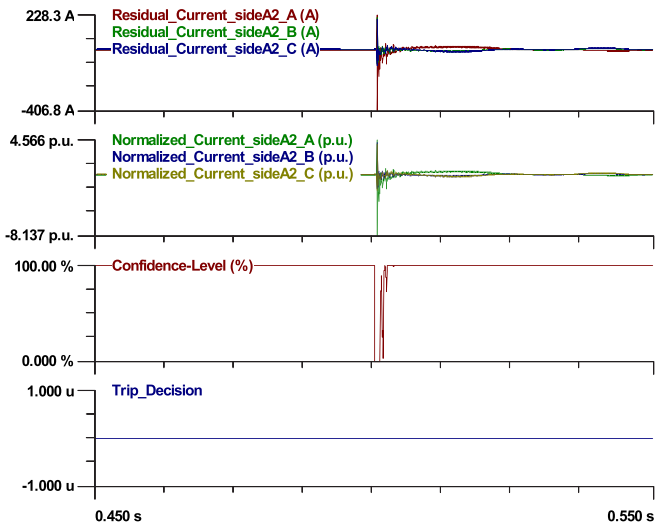

Fig. 14. EBP results of a phase A to ground external fault at bus A1, bus-side relay installation.

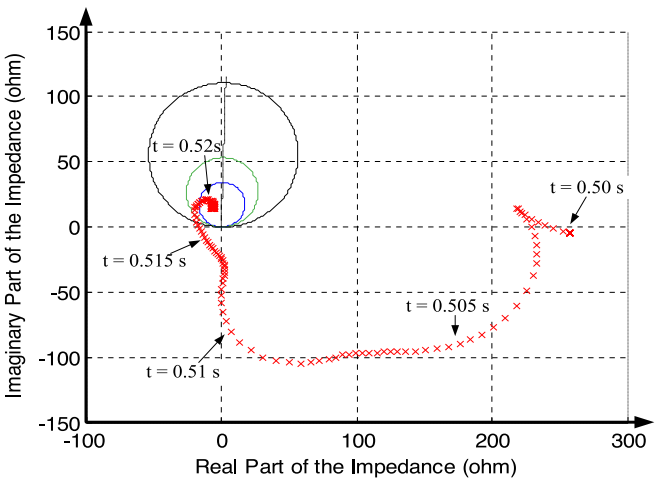

Fig. 15. Trace of impedance during a phase A to ground internal fault near SCs, line-side relay installation.

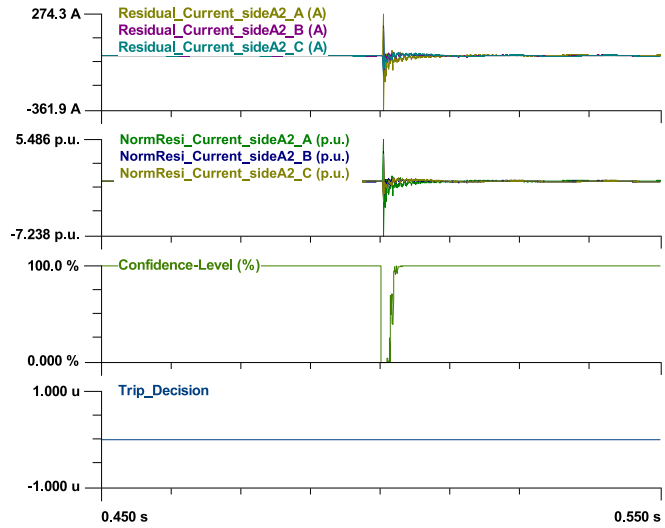

Fig. 16. EBP results of a phase A to ground external fault at bus A1, line-side relay installation.

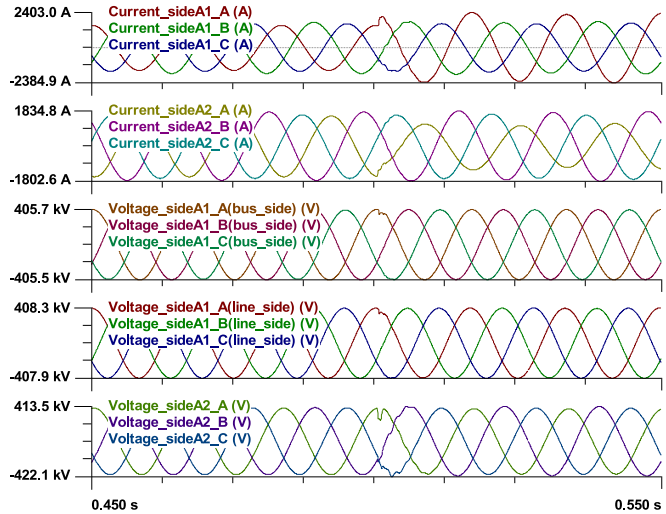

Fig. 17. Current and voltage results of a phase A to ground high impedance internal fault.

EBP relay: The results are depicted in Fig. 14. The confidence level stays at 100% except some transients for a short period (around 1.5 ms). The trip signal remains at zero. Thus, the EBP relay correctly ignores this external fault.

Summary: For event 2 and **bus-side relay installation**, legacy protection relays and EBP relay correctly ignore the external fault.

Performance of Line-side Relay Installation

Distance protection relay: the impedance "seen" by the relay, superimposed on its characteristic, is shown in Fig. 15. The impedance enters zone 1 of the characteristic. Thus, the distance relay will wrongly trip the line at $0.519 + 0.015$ s $= 0.534$ s.

Line differential protection relay: the performance is the same as in Fig. 13. The relay will correctly ignore this external fault.

EBP relay: The results are depicted in Fig. 16. The confidence level stays at 100% except some transients for a short period (around 1.5 ms). Thus, the EBP relay correctly ignores this external fault.

Summary: For event 2 and **line-side relay installation**, distance protection incorrectly trips the line at 0.534 s, while line differential and the EBP relay correctly ignore the external fault.

C. Event 3: High Impedance Phase A-G Internal Fault

A phase A to ground internal fault with 300 Ω impedance occurs at 60 miles from the side A1 and time 0.5 s. The results are shown in Fig. 17 for the period [0.45 s to 0.55 s].

Performance of Bus-side Relay Installation

Distance protection relay: the impedance "seen" by the relay, superimposed on its characteristic, is shown in Fig. 18. The impedance stays outside of the relay characteristic. Thus, the distance relay fails to detect this fault.

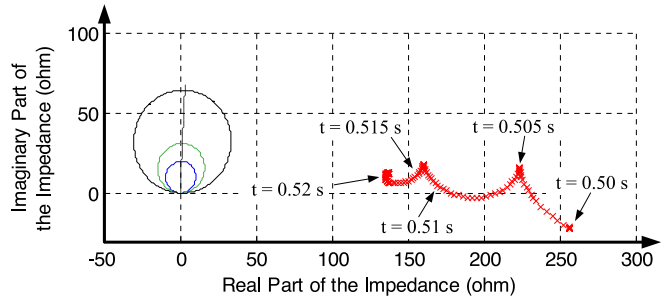

Fig. 18. Trace of impedance during a phase A to ground high impedance internal fault, bus-side relay installation.

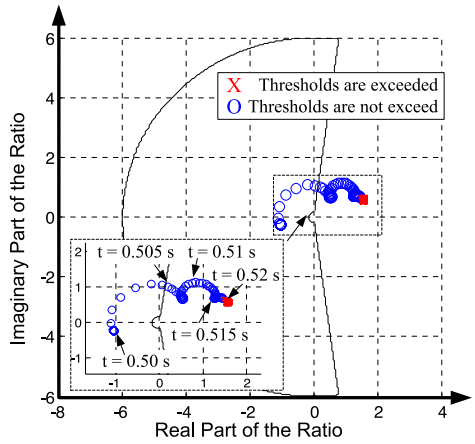

Fig. 19. Trace of ratio during a phase A to ground high impedance internal fault, bus-side relay installation.

Line differential protection relay: the phasor ratio trace of zero sequence current, superimposed on the relay characteristic, is shown in Fig. 19. Prior to the fault, the ratio is in the restraint region, and none of the thresholds are exceeded (character 'o'). During the fault, the ratio exits the restraint region at 0.504 s and the threshold asserts (character 'x') at 0.520 s. The line is tripped at $0.520 + 0.015$ s $= 0.535$ s.

EBP relay: The results are depicted in Fig. 20. The confidence level drops to near zero 0.2 ms after the fault initiation. The trip command is issued at 0.5154 s.

Summary: For event 3 and **bus-side relay installation**, distance relay fails to detect the fault; differential relay and EBP relay issue a trip command at 0.535 s and 0.5154 s respectively.

Performance of Line-side Relay Installation

Distance protection relay: the impedance "seen" by the relay, superimposed on its characteristic, is shown in Fig. 21. The impedance stays outside the tripping characteristic. Thus, the distance relay fails to detect this fault.

Line differential protection relay: the performance is the same as in Fig. 19. The relay issues a trip at time 0.535 s.

EBP relay: The results are depicted in Fig. 22. The EBP relay detects the fault at 0.5002 s and issues a trip at 0.5153 s.

Summary: For event 3 and **line-side relay installation**, distance protection relay fails to detect the fault; line differential relay detects the fault at 0.520 s and issues a trip at 0.535 s; EBP relay detects the fault at 0.5002 s and issues a trip at 0.5153 s.

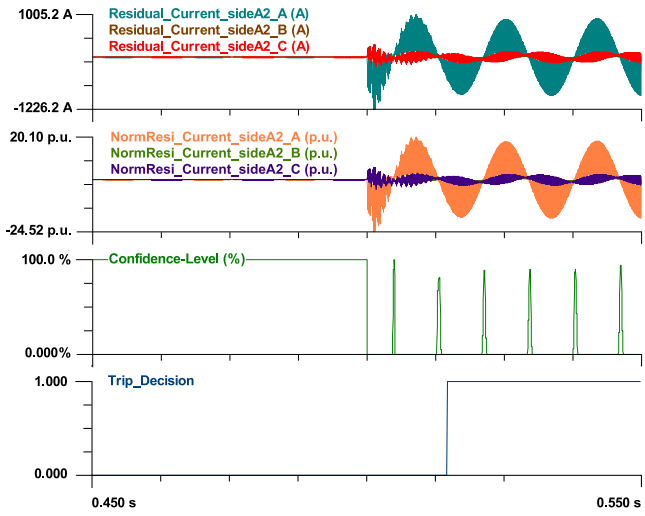

Fig. 20. EBP results of a phase A to ground high impedance internal fault, bus-side relay installation.

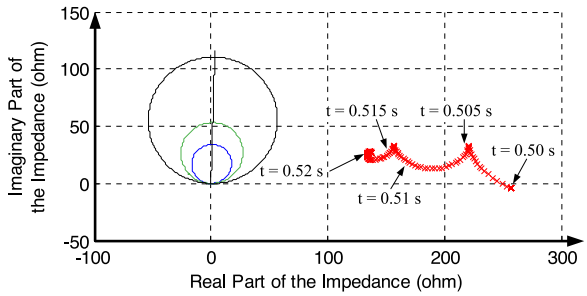

Fig. 21. Trace of impedance during a phase A to ground high impedance internal fault, line-side relay installation.

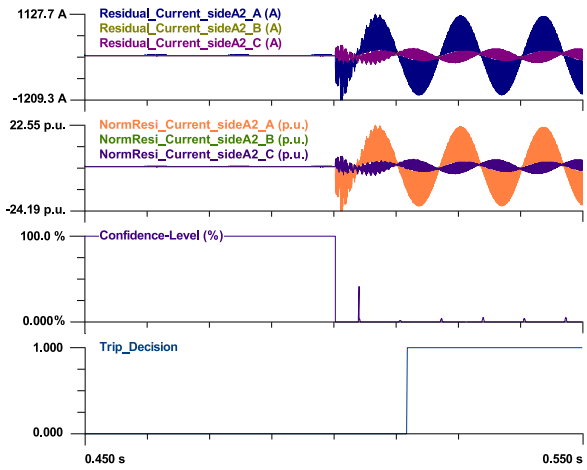

Fig. 22. EBP results of a phase A to ground high impedance internal fault, line-side relay installation.

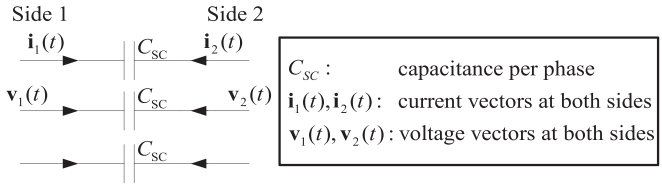

Fig. A-1. Series capacitors model.

D. Influence of MOVs

The Metal Oxide Varistors (MOVs) protect SCs from overvoltage. MOVs are selected to operate when the voltage across the capacitors exceed a certain value. This corresponds to a certain fault current which can be exceeded for certain external system configuration and on-line generating sources. In this case of substantial conduction in the MOVs, the equivalent impedance of the SCs/MOVs changes, affecting fault currents and possibly leading to operation of the bypass air gaps. To deal with these issues, legacy distance protection schemes use memory polarization. The method provides a better polarization voltage for a short time in cases of MOV conduction and/or air gap flashover during internal faults [6]. It is important to note that during coincidental transients with the fault, the correct polarizing voltage shifts and will compromise this method. Also, the equivalent impedance of SCs/MOVs varies as MOV conduction level changes [15]. On the other hand, the performance of line differential protection is not affected by MOV conduction or air gap sparkover. Similarly, the proposed EBP is not affected by these issues. While we have not presented cases in which the MOV conducts due to space limitations, we will do so in future publications.

VII. Conclusion

Series compensated lines bring benefits but also protection challenges due to discontinuity of the inductive impedance from SCs. The paper proposes a new Dynamic State **E**stimation **B**ased **P**rotection (EBP) that overcomes the limitations of legacy protection functions. The method requires a high fidelity dynamic model of the series compensated line and GPS synchronized measurements at the two ends of the line. Dynamic state estimation is used to determine how well the measurements fit the dynamic model of the series compensated line and quantifies the fit with the confidence level. The confidence level is close to 1.0 for normal operation or external faults and drops to zero during internal faults in which case a trip command is issued. The performance of the EBP method, as applied to series compensated lines, has been evaluated and compared with legacy protection schemes via numerical simulations. The advantages of the proposed scheme include: (a) it simplifies the settings of the protection and does not need coordination with other protection functions; (b) it detects faults faster than legacy protection schemes (within sub-millisecond); (c) it is immune to current inversion due to SCs; and (d) it detects high impedance faults dependably and securely.

In this paper, we have not provided results of the effect of measurement errors on the performance of the method due to space limitations. Numerical results with multiple fault cases and with injected random error of 0.1% to 1% indicate no deterioration of the performance of the method. It is recognized that most of the measurement error comes from the instrumentation channel (instrument transformers, control cables, burdens, etc.) and it is systematic rather than random. We have modeled the instrumentation channels and have studied their effects on the EBP relay. These results will be published in a follow-up publication.

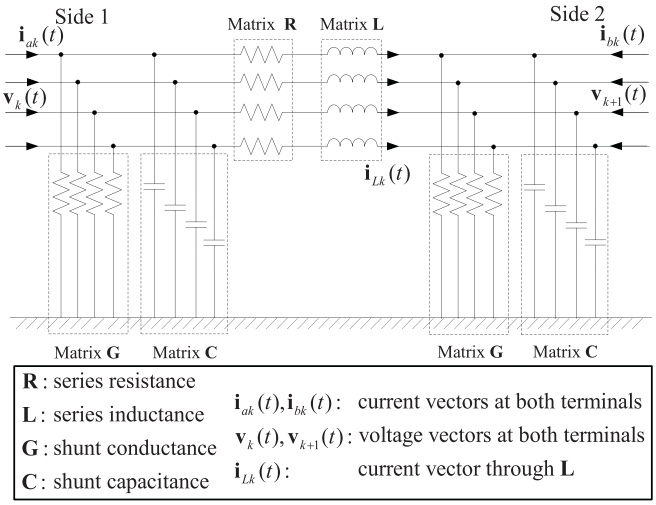

Fig. A-2. π-equivalent line section model (mutual inductances and capacitances are not shown).

Appendix A
Device QDM of Series Capacitors and π-Equivalent Transmission Line Section

This Appendix describes the QDM of SCs and π-equivalent transmission line section. Fig. A-1 shows the model of SCs.

$$\mathbf{D}_{eqxd1} = \begin{bmatrix} diag[C_{\rm SC}\ \ C_{\rm SC}\ \ C_{\rm SC}] & -diag[C_{\rm SC}\ C_{\rm SC}\ C_{\rm SC}] \\ -diag[C_{\rm SC}\ \ C_{\rm SC}\ \ C_{\rm SC}] & diag[C_{\rm SC}\ C_{\rm SC}\ C_{\rm SC}] \end{bmatrix}$$

all other vectors and matrices are null;

The QDM of SCs are: $\mathbf{i}(t) = [\mathbf{i}_1(t)\ \mathbf{i}_2(t)]^{\rm T}$; $\mathbf{x}(t) = [\mathbf{v}_1(t)\ \mathbf{v}_2(t)]^{\rm T}$;

Fig. A-2 shows a π-equivalent model of a line section. The QDM of section k inside multi-section transmission lines are: $\mathbf{i}(t) = [\mathbf{i}_1(t)\ \mathbf{i}_2(t)]^{\rm T}$; $\mathbf{x}(t) = [\mathbf{v}_1(t)\ \mathbf{v}_2(t)\ \mathbf{i}_L(t)]^T$; $\mathbf{Y}_{eqx2} = [-\mathbf{I}_n\ \mathbf{I}_n\ \mathbf{R}]$;

$$\mathbf{Y}_{eqx1} = \begin{bmatrix} \mathbf{G} & \mathbf{0} & \mathbf{I}_n \\ \mathbf{0} & \mathbf{G} & -\mathbf{I}_n \end{bmatrix}; \mathbf{D}_{eqx1} = \begin{bmatrix} \mathbf{C} & \mathbf{0} & \mathbf{0} \\ \mathbf{0} & \mathbf{C} & \mathbf{0} \end{bmatrix};$$

$$\mathbf{D}_{eqx2} = \begin{bmatrix} \mathbf{0} & \mathbf{0} & \mathbf{L} \end{bmatrix};$$

; all other vectors and matrices are null; and $\mathbf{I}_n$ is the identity matrix with dimension n, where n is the number of conductors of the transmission line. For three-phase transmission lines, n is equal to 4 or 5 with one or two neutral conductors.

REFERENCES

[1] A. Newbould and I. A. Taylor, "Series compensated line protection: System modeling and relay testing," in *Proc. 4th Int. Conf. Develop. Power Protection*, 1989, pp. 182–186.

[2] A. K. Pradhan, A. Routray, S. Pati, and D. K. Pradhan, "Wavelet fuzzy combined approach for fault classification of a series-compensated transmission line," *IEEE Trans. Power Del.*, vol. 19, no. 4, pp. 1612–1618, Oct. 2004.

[3] N. Perera and A. D. Rajapakse, "Series-compensated double-circuit transmission- line protection using directions of current transients," *IEEE Trans. Power Del.*, vol. 28, no. 3, pp. 1566–1575, Jul. 2013.

[4] M. M. Saha, B. Kastenny, E. Rosolowski, and J. Izykowski, "First zone algorithm for protection of series compensated lines," *IEEE Trans. Power Del.*, vol. 16, no. 2, pp. 200–207, Apr. 2001.

[5] T. S. Sidhu and M. Khederzadeh, "Series compensated line protection enhancement by modified pilot relaying schemes," *IEEE Trans. Power Del.*, vol. 21, no. 3, pp. 1191–1198, Jul. 2006.

[6] H. J. Altuve, J. B. Mooney, and G. E. Alexander, "Advances in series-compensated line protection," in *Proc. 2009 62nd Annu. Conf. Protective Relay Eng.*, Austin, TX, USA, Mar. 2009, pp. 263–275.

[7] S. He, J. Suonan, and Z. Q. Bo, "Integrated impedance-based pilot protection scheme for the TCSC-compensated EHV/UHV transmission lines," *IEEE Trans. Power Del.*, vol. 28, no. 2, pp. 835–844, Apr. 2013.

[8] A. P. Meliopoulos, G. J. Cokkinides, Z. Tan, S. Choi, Y. Lee, and P. Myrda, "Setting-less protection: Feasibility study," in *Proc. 46th Hawaii Int. Conf. Syst. Sci.*, Maui, HI, USA, Jan. 2013, pp. 2345–2353.

[9] R. Huang, E. Farantatos, G. J. Cokkinides, and A. P. S. Meliopoulos, "Substation based dynamic state estimator-numerical experiment," in *Proc. IEEE Power Energy Soc. Transmiss. Distrib. Conf. Expo.*, New Orleans, LA, USA, 2010, pp. 1–8.

[10] Y. Liu, A. P. S. Meliopoulos, R. Fan, and L. Sun, "Dynamic state estimation based protection of microgrid circuits," in *Proc. IEEE Power Energy Soc. Gen. Meet.*, Denver, CO, USA, 2015, pp. 1–5.

[11] R. Fan, A. P. S. Meliopoulos, L. Sun, and Y. Liu, "Dynamic state estimation-based protection of power transformers," in *Proc. IEEE Power Energy Soc. Gen. Meet.*, Denver, CO, USA, 2015, pp. 1–5.

[12] A. P. Meliopoulos, G. J. Cokkinides, and G. K. Stefopoulos, "Quadratic integration method," in *Int. Power Syst. Transients Conf.*, Montreal, Canada, 2005.

[13] F. C. Schweppe and R. D. Masiello, "A tracking static state estimator," *IEEE Trans. Power App. Syst.*, vol. PAS-90, no. 3, pp. 1025–1033, May 1971.

[14] *SEL-387L Relay Instruction Manual*, Schweitzer Engineering Laboratories, Inc., Pullman, WA, USA, 2011.

[15] D. L. Goldsworthy, "Linearized model for MOV-protected series capacitors," *IEEE Trans. Power Syst.*, vol. 2, no. 4, pp. 953–958, Nov. 1987.

[16] *IEEE Guide for Application of Digital Line Current Differential Relays Using Digital Communication*, IEEE Std C37.243-2015, Aug. 7, 2015.

[17] E. Sagen and K. Workman, "Methods of time synchronization," in *63rd Georgia Tech. Protective Relay Conf.*, Atlanta, GA, USA, Apr. 2009.

Yu Liu (S'13) was born in Hefei, China, in 1990. He received the B.S. and M.S. degrees in electric power engineering from Shanghai Jiao Tong University, Shanghai, China, in 2011 and 2013, respectively, and the M.S. degree in electrical and computer engineering from Georgia Institute of Technology, Atlanta, GA, USA, in 2013. He is currently working toward the Ph.D. degree in the Department of Electrical and Computer Engineering, Georgia Institute of Technology.

His research interests include power system protection, parameter estimation, and circuit fault locating.

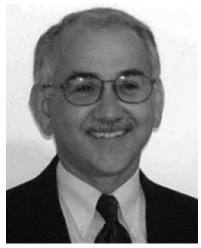

A. P. Sakis Meliopoulos (M'76–SM'83–F'93) was born in Katerini, Greece, in 1949. He received the M.E. degree and E.E. diploma from the National Technical University of Athens, Greece, in 1972, and the M.S.E.E. and Ph.D. degrees from the Georgia Institute of Technology, Atlanta, GA, USA, in 1974 and 1976, respectively.

He joined the Faculty of Electrical Engineering, Georgia Institute of Technology in 1976, where he is currently Georgia Power Distinguished Professor. He holds three patents, published three books and more than 350 technical papers.

Dr. Meliopoulos received the IEEE Richard Kaufman Award in 2005, he received the IEEE Richard Kaufman Award and received the George Montefiori Award in 2010. He is the Chairman of the Georgia Tech Protective Relaying Conference and a member of Sigma Xi.

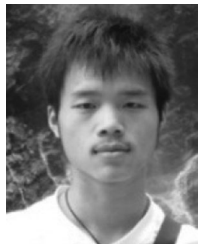

Rui Fan (S'12) was born in Wuhan, China in 1989. He received the B.S. and M.S. degrees in electrical engineering from Huazhong University of Science and Technology, Huazhong, China, in 2011 and from Georgia Institute of Technology, Atlanta, GA, USA, in 2012, respectively.

He is currently with Pacific Northwest National Laboratory. His research interests include power electronics, power system protection, reliability analysis, and microgrid autonomous operation.

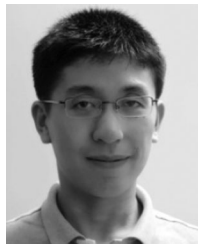

Liangyi Sun (S'12) received the B.S. degree in electrical power engineering from Shanghai JiaoTong University, Shanghai, China, in 2010 and the M.S. degree in electrical and computer engineering from Georgia Institute of Technology, Atlanta, GA, USA, in 2012. He is currently working toward the Ph.D. degree in the Department of Electrical and Computer Engineering, Georgia Institute of Technology.

His research interests include power system protection, transient stability, and wind power control.

Zhenyu Tan (S'12) received the B.E. degree in electrical engineering from Tsinghua University, Beijing, China, in 2011. He is currently working toward the Ph.D. degree at Georgia Institute of Technology, Atlanta, GA, USA.

His research interests include power system generator protection and control and distributed power system automation.